X80 级管线钢三丝埋弧焊接热过程的数值分析

赵　明，　王海燕，　万夫伟，　罗德通
（中国石油大学（华东）机电工程学院，青岛　266580）

摘　要： 针对 X80 级高强管线钢纵向焊缝三电极串列三丝埋弧焊，借助 ANSYS 有限元分析软件，采用生死单元技术处理双 V 形坡口填充，利用双椭球体积热源分布模式实现载荷的施加与求解，建立焊接热过程数值分析模型. 计算结果表明，焊接开始后 1.6 s 时出现三电极共熔池现象，到 5 s 时焊接过程达到准稳态，形成长度逾 100 mm 的熔池；焊缝区和 HAZ 的焊接热循环曲线出现三个高温波峰，延长了热循环曲线的高温停留时间，是 HAZ 晶粒粗化和焊接接头性能劣化的主要诱因. 焊接工艺试验与数值计算结果对比表明，熔宽比熔深吻合更加良好，考虑焊缝余高可进一步提高计算精度.

关键词： 管线钢；　多丝埋弧焊；　热影响区；　热循环曲线；　数值模拟
中图分类号： TG 445　　**文献标识码：** A　　**文章编号：** 0253－360X(2014)10－0017－04

0　序　　言

随着世界各国对油气资源需求的增加，将油气资源跨越成百上千公里输送到人口密集的炼化厂和用户，是一项关系国计民生的重大工程. X70 以上高钢级管线钢材在石油和天然气长距离远程输送工程中的应用，可显著降低油气资源的输送成本和提高输送安全性[1－3]. 而焊接工艺是管线钢从板材加工成管材、从筒体连接成管道的必要环节. 随着管线钢强度级别的进一步提高，焊接热影响区(HAZ)晶粒粗化和焊接接头性能软化的问题就越来越严重[4－6].

文中通过焊接工艺试验和数值分析技术相结合，研究 X80 级高强管线钢三丝埋弧焊接热过程中焊接温度场的瞬态演变和工件上一系列点的焊接热循环，并通过分析焊接热影响区热循环特征参数，揭示 HAZ 晶粒粗化和焊接接头性能劣化的产生机制. 可为进一步优化 X80 级和 X80 级以上管线钢的焊接工艺参数，以及改善焊接接头性能提供理论依据和基础数据，具有重要的理论意义和工程实用价值.

1　焊接方法

试验用 X80 级高强管线钢厚度 15.3 mm，焊丝直径 4.0 mm，其主要化学成分见表 1，余量为 Fe. 焊前工件按照图 1 进行坡口加工. 采用三电极三丝串列埋弧焊接工艺，主要工艺参数见表 2. 图 2 是焊接接头横截面宏观金相形貌.

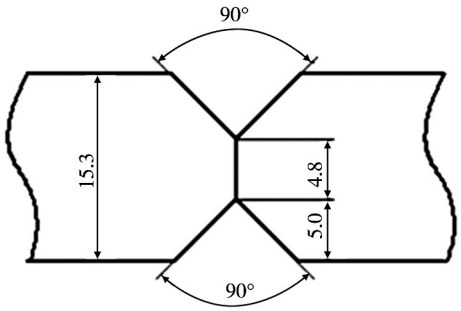

图 1　坡口形状(mm)
Fig. 1　Double-V groove

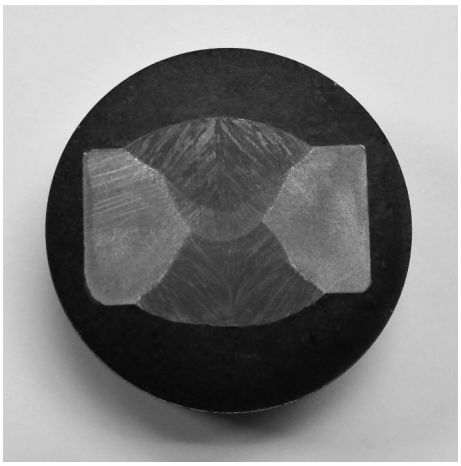

图 2　焊缝横截面光学形貌
Fig. 2　Macrograph for cross section of weld bead

收稿日期：2013－04－28
基金项目：国家自然科学基金资助项目(51305461)；中央高校基本科研业务费专项资金资助项目(13CX02075A)；中国石油大学(华东)研究生创新基金资助项目(CX2013048)

表 1 母材和焊丝的主要化学成分(质量分数,%)

Table 1 Chemical compositions of base metal and weld consumable

	C	Mn	Si	P	S	Mo	Ni	Cr	Cu	V	Nb	Ti	Al	N	B
母材	0.072	1.805	0.250	0.007 8	0.001	0.29	0.260	0.02	0.009	0.003 0	0.035	0.012	0.031	0.004	—
焊丝	0.056	1.610	0.290	0.014 0	0.002	0.15	0.047	0.15	2.490	0.006 8	0.038	0.014	0.018	—	0.001 8

表 2 主要焊接工艺参数

Table 2 Main parameters for welding process

焊丝编号	焊接电流 I/A	电弧电压 U/V	焊接速度 v_0/(mm·s^{-1})	电流类型	焊丝间距 d/mm	焊枪倾角 α/(°)
1	800	32	17.79	直反		−15
2	450	34	17.79	交流	18	15
3	450	38	17.79	交流	22	25

2 数学模型

文中未考虑 X80 级管线钢纵向焊缝焊接前从板材卷制成管材的变形,制管时先在管道的下部焊接内焊道,而当已经焊好内焊道的坡口旋转到顶部时再焊接外焊道,因此纵缝焊接可简化为平板对接焊. 直角坐标系中焊接热传导控制方程为

$$\rho(T)\,c_p(T)\frac{\partial T}{\partial t}=\frac{\partial}{\partial x}\left[k(T)\frac{\partial T}{\partial x}\right]+\frac{\partial}{\partial y}\left[k(T)\frac{\partial T}{\partial y}\right]+\frac{\partial}{\partial z}\left[k(T)\frac{\partial T}{\partial z}\right]+q \tag{1}$$

式中: ρ 为密度; c_p 为比热容; k 为热导率; T 为温度; t 为时间; q 为热源项; x 方向为焊接方向; y 方向为焊缝横截面方向; z 方向为工件厚度方向.

三电极三丝串列埋弧焊接工艺,由于焊接电弧间距比较大,因此每个焊接电弧都可以单独采用三维双椭球体积热源分布模式[7] 如图 3 所示,数学表达式为

$$x\geqslant 0,\ q_f(x,y,z,t)=\frac{6\sqrt{3}f_f\eta UI}{\pi\sqrt{\pi}a_1bc}\times\exp\left(-\frac{3(x-x_0-v_0t)^2}{a_1^2}-\frac{3(y-y_0)^2}{b^2}-\frac{3(z-z_0)^2}{c^2}\right) \tag{2}$$

$$x<0,\ q_r(x,y,z,t)=\frac{6\sqrt{3}f_r\eta UI}{\pi\sqrt{\pi}a_2bc}\times\exp\left(-\frac{3(x-x_0-v_0t)^2}{a_2^2}-\frac{3(y-y_0)^2}{b^2}-\frac{3(z-z_0)^2}{c^2}\right) \tag{3}$$

式中: η 电弧热效率; 点 $O(x_0, y_0, z_0)$ 为电弧中心位置坐标; a_1, a_2, b, c 分别为双椭球体积热源三维形状分布参数(不同热源的分布参数各不相同); f_f, f_r 分别为总的焊接热输入功率在熔池前后两部分的能量分布系数,满足下列关系式

$$f_f+f_r=2 \tag{4}$$

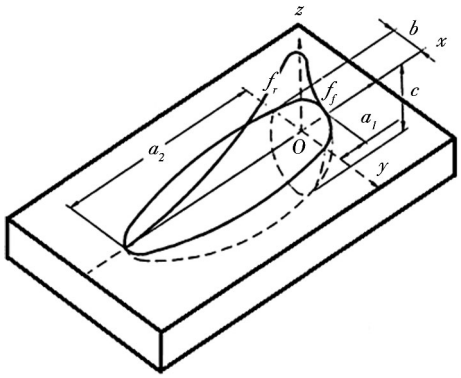

图 3 双椭球体积热源模型

Fig. 3 Double-ellipsoid volumetric heat source model

焊接初始条件为

$$T(x,y,z,0)=T_a \tag{5}$$

式中: T_a 为环境温度; 文中赋值为 20 ℃.

ANSYS 中使用一个总换热系数来同时考虑对流和辐射边界条件,数学表达式为

$$q_t=\alpha(T-T_a) \tag{6}$$

式中: q_t 为对流和辐射总热流损失; α 为对流和辐射总换热系数.

ANSYS 中采用热焓法处理相变潜热,即通过定义材料随温度变化的焓来考虑潜热. 焓值可描述为密度、比热以及温度的函数,数学关系式为

$$\Delta H=\int\rho(T)\,c_p(T)\,\mathrm{d}T \tag{7}$$

将实体模型采用映射网格划分为有限元模型,单元尺寸 0.9 mm,借助生死单元技术处理坡口填充. 3 个焊接电弧中心坐标分别为: O_3(0.018,0,0), O_2(0.036,0,0), O_1(0.058,0,0),采用加速步长法反演双椭球体热源模型分布参数[8],利用三维数组定义任一时刻生热率在工件上的分布.

3　计算结果与讨论

3.1　焊接温度场

温度场的三维动态演变如图 4 所示,分别从工件上表面和焊缝纵截面展示了从 0.5 ~ 5 s(时间间隔为 0.5 s) 不同时刻的焊接温度场分布. 从图 4 中可见,当 t = 0.5 s 时,工件上出现 3 个各自独立的高温区域,前弧已经在工件上形成微小的熔池; 到 t = 1.0 s 时,前弧和中间弧开始出现共熔池现象; t = 1.6 s 时,开始出现三电弧共熔池现象; 此后随着焊接过程的继续进行,由于前弧对后弧的预热效应,三丝共熔池现象更加明显,熔池拉长,熔深增加,到 t = 4.0 s 左右焊接过程达到准稳定状态.

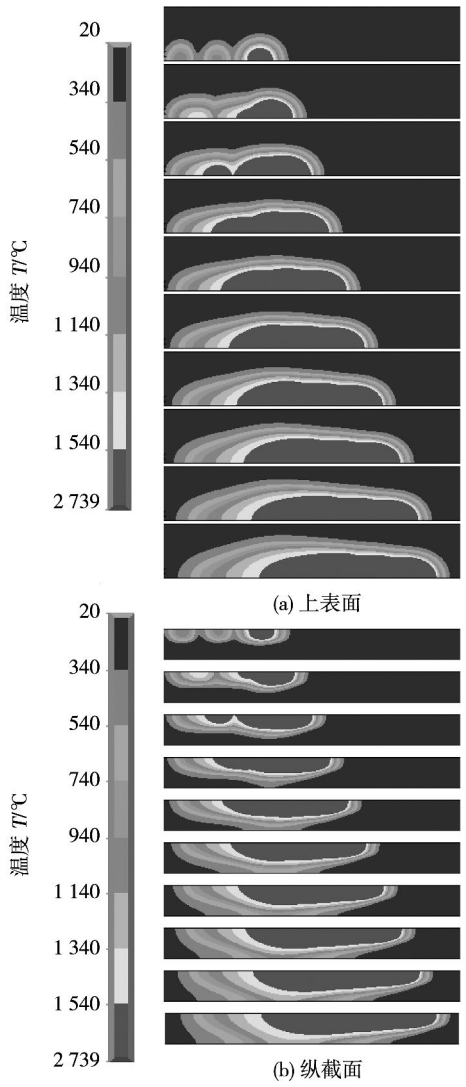

图 4　焊接温度场的瞬态演变

Fig. 4　Evolution of temperature field

3.2　焊接热循环曲线

图 5 是沿工件不同方向排列的一系列点的焊接热循环曲线. 从图 5a 可见,后弧中心点 O_3(0.018, 0,0) 只经历一个焊接电弧的作用,焊接热循环曲线与普通埋弧焊相似,只出现 1 个高温波峰; 中间电弧中心点 O_2(0.036,0,0) 经历中间弧和后弧的作用,焊接热循环曲线出现 2 个高温波峰; 前弧中心点 O_1(0.058,0,0) 经历 3 个焊接电弧的作用,焊接热循环曲线出现 3 个高温波峰; 而位于 O_3 和 O_2 之间的点,如图 5a 中的点 P_{32}(0.027,0,0) ,只经历最后一个焊接电弧的作用而出现 1 个高温波峰; 位于 O_2 和 O_1 之间的点,如图 5a 中的点 P_{21}(0.047,0,0) ,经历后弧和中间弧的作用而出现 2 个高温波峰; 位于 O_1 之前的点,如图 5a 中的点 P_1(0.094,0,0) 和点 P_0(0.13,0,0) ,经历 3 个焊接电弧的作用而出现 3 个高温波峰.

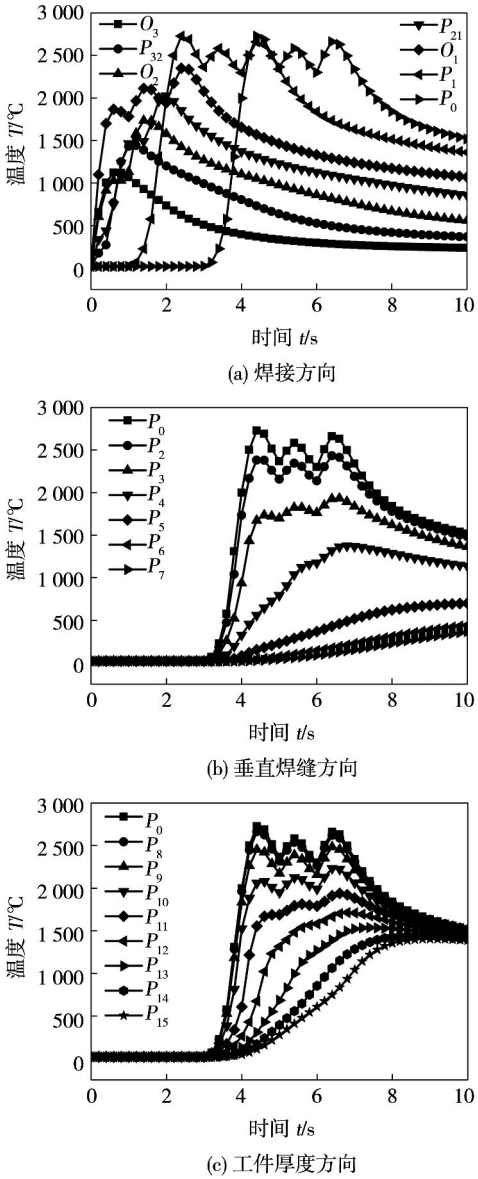

图 5　焊接热循环曲线

Fig. 5　Welding thermal cycles

图 5b 是沿垂直焊缝方向一系列等距离点的焊接热循环曲线. 从焊缝中心线上的点 P_0(0.13,0,0) 到工件边沿的点 P_7(0.13,0.027,0),沿工件宽度方向的间距依次增加 4.5 mm,焊接热循环曲线从中心线上的点 P_0 出现 3 个明显的高温波峰,点 P_2(0.130,0.0045,0) 和点 P_3(0.130,0.009,0) 的高温波峰逐渐递减,到点 P_4(0.130,0.0135,0) 只有微小的温度波动. 与焊缝中心线距离大于 13.5 mm 的点,三电弧对其焊接热循环曲线不产生波动效应.

图 5c 是沿工件厚度方向排列的一系列等距离点的焊接热循环曲线. 从位于工件上表面的点 P_0(0.13,0,0) 到位于工件下表面的点 P_{15}(0.13,0,−0.015 3),每个点沿工件厚度方向增加 1.8 mm. 从图 5c 可见,位于点 P_{10}(0.13,0,−0.005 4) 以上区域的点的焊接热循环曲线,都会出现 3 个明显的高温波峰; 位于点 P_{13}(0.13,0,−0.010 8) 以下区域的点,三电弧对其焊接热循环曲线高温区的影响效果也不明显; 而介于点 P_{10}(0.13,0,−0.005 4) 和点 P_{13}(0.13,0,−0.010 8) 之间的点,其焊接热循环曲线的高温峰值明显降低,峰值温度区间仅有微小的温度波动.

3.3 焊接热影响区

分析图 5 中的焊接热循环曲线发现,三电弧的作用虽然没有提高峰值温度,但明显延长了相变温度以上的停留时间. 尤其是对于焊接热影响区,高温停留时间的延长,会促使母材晶粒长大,劣化焊接热影响区的力学性能,严重时会使焊接热影响区强度明显下降,导致焊接接头软化. 因此,需要对焊接工艺参数进行优化以控制焊接热输入,防止焊接热影响区晶粒粗化现象的产生.

3.4 试验验证

计算结果表明,当 t = 10 s 时,熔池在三维空间几何形状的极值分别为: 熔池长度 107.0 mm,最大熔宽 25.2 mm,最大熔深 10.8 mm. 分析图 2 中的焊缝横截面金相图,可得焊缝宽度为 25.0 mm,与计算结果 25.2 mm 吻合良好; 试验熔深为 9.1 mm,比计算结果最大熔深 10.8 mm 小 1.7 mm. 误差产生的主要原因是文中所建立模型尚未考虑焊缝余高和流体流动,作者在后续研究中将予以改进.

4 结 论

(1) 采用三维双椭球体积热源分布模式,建立了三电极三丝串列埋弧焊接热过程的数值分析模型,利用生死单元技术处理坡口填充,基于 ANSYS 平台实现了载荷的施加与求解.

(2) 分析了 X80 级高强管线钢三丝埋弧焊接热过程中焊接温度场的瞬态演变和焊接热循环曲线,并通过对 HAZ 热循环特征参数的分析,揭示了 HAZ 晶粒粗化和焊接接头性能劣化的产生机制.

(3) 开展了焊接工艺试验,并将计算结果与试验结果进行了对比验证,分析了误差产生的主要原因,提出了提高数值分析精度的措施.

参考文献:

[1] 王晓香. 超高强度管线钢管研发新进展[J]. 焊管, 2010, 33(2): 5 − 12.
Wang Xiaoxiang. Development progress of pipeline steel with extra-high strength [J]. Pipeline, 2010, 33(2): 5 − 12.

[2] Kondo K, Aral Y, Hirata H, *et al*. Development of high strength heavy wall seamless pipes of X80-X100 grade for ultra-deep water application [C] // International Pipeline Conference, Calgary, 2008: 49 − 59.

[3] Hillenbrand H G, Liessem A, Knauf G, *et al*. Development of high strength material and pipe production technology for grade X120 line pipe [C] // International Pipeline Conference, Calgary, 2004: 1743 − 1749.

[4] Moeinifar S, Kokabi A H, Madaah Hosseini H R. Role of tandem submerged arc welding thermal cycles on properties of the heat affected zone in X80 microalloyed pipe line steel [J]. Journal of Materials Processing Technology, 2011, 211(9): 368 − 375.

[5] Kiran D V, Basu B, De A. Influence of process variables on weld bead quality in two wire tandem submerged arc welding of HSLA steel [J]. Journal of Materials Processing Technology, 2012, 212(10): 2041 − 2050.

[6] Tian S Y, Yan C Y, Zhao X, *et al*. Effect of parameters on temperature field during twin-wire submerged arc welding of X80 pipeline steel [J]. Advanced Materials, 2013, 652/654: 2347 − 2351.

[7] Goldak J, Chakravarti A, Bibby M. A new finite element model for welding heat sources [J]. Metallurgical Transaction B, 1984, 15(6): 299 − 305.

[8] 郭晓凯, 李培麟, 陈俊梅, 等. 加速步长法反演多丝埋弧焊双椭球热源模型参数[J]. 焊接学报, 2009, 30(2): 53 − 56.
Guo Xiaokai, Li Peilin, Chen Junmei, *et al*. Inversing parameter values of double ellipsoid source model during multiple wires submerged arc welding by using step acceleration method [J]. Transactions of the China Welding Institution, 2009, 30(2): 53 − 56.

作者简介: 赵 明,女,1973 年出生,博士,副教授,硕士研究生导师. 主要从事焊接过程数值分析与新材料连接技术方面的科研和教学工作. 发表论文 20 余篇. Email: zhaoming08@upc.edu.cn

MAIN TOPICS, ABSTRACTS & KEY WORDS

Development of self-shielded flux cored wire for X100 pipeline steel and performance analysis of welded joints

ZHANG Min, LIU Mingzhi, CHEN Yangyang, LI Jihong (College of Material Science and Engineering, Xi'an University of Technology, Xi'an 710048, China). pp 1 - 4

Abstract: The alloy systems of weld metal of X100 pipeline steel were determined with the principle of composition match and structure match. Combined with the principle of weld metal alloying, the types and content of alloy elements which need to transit in the weld can be quantitatively calculated, based on which the flux-cored wire match to X100 pipeline steel was designed and made. The appropriate welding process parameters for welding and the according joint performance were also analyzed. The results showed that the flux-cored wire has excellent mechanical properties with the tensile strength up to 795 MPa, yield strength up to 615 MPa and impact energy value to 47.7J(-40 ℃). The microstructure of the weld metal consists of lath bainite, granular bainite, and little acicular ferrite, which can match well with base material.

Key words: X100 pipeline steel; flux-cored wire; self-shielded; mechanical properties; alloying

Effects of longitudinal magnetic field on non-consumable gas shielded arc welding

CHEN Shujun[1], MENG Danyang[2], SU Zaiwei[2], JIANG Fan[1], LU Yongsheng[1] (1. College of Mechanical Engineering and Applied Electronics Technology, Beijing University of Technology, Beijing 100124, China; 2. Tianjin Aerospace Long March Rocket Manufacturing Co. Ltd., Tianjin 300462, China). pp 5 - 8

Abstract: Based on theoretical analysis and experimental method, a set of parallel longitudinal magnetic field generating device is used on the non-consumable gas shielded arc welding process, which includes plasma arc welding and tungsten arc welding. With the use of a high-speed video camera observation the arc shape are measured. Then the arc changes of the two kinds of welding method under the longitudinal magnetic field are compared. The experiment results refer that owing to the specificeness of the composition of the plasma arc, the differences between the two kinds of the welding method under the same magnetic field occur. And by means of making analysis of the movement of the particle, the particle motion model is established under the longitudinal magnetic field. It illustrates that because of the difference of the longitudinal velocity of the particles the difference of the motion stage of the charged particles under the longitudinal magnetic field will appear, which explains that why the difference of the arc shape changes exists between the two non-consumable gas shielded arc welding under the same magnetic field.

Key words: longitudinal magnetic field; non-consumable gas shielded arc welding; arc force analysis; particle motion model

Effect of bonding temperature on interfacial microstructure and properties of $TiAl/Ti_3AlC_2$ joint

SONG Xiaoguo[1,2], WANG Meirong[2], LIN Xingtao[1], LIU Jiakun[1], CAO Jian[1,2], FENG Jicai[1,2] (1. State Key Laboratory of Advanced Welding and Joining, Harbin Institute of Technology, Harbin 150001, China; 2. Shandong Provincial Key Laboratory of Special Welding Technology, Harbin Institute of Technology at Weihai, Weihai 264209, China). pp 9 - 12

Abstract: Diffusion bonding of TiAl alloy and Ti_3AlC_2 ceramic was achieved by using Ti/Ni composite interlay. The interfacial microstructure of $TiAl/Ti_3AlC_2$ joint was analyzed by SEM, EDS and XRD, and was determined as $TiAl/Ti_3Al + Al_3NiTi_2/Ti_3Al/\alpha$-Ti + $Ti_2Ni/Ti_2Ni/TiNi/Ni_3Ti/Ni/Ni_3(Ti, Al)/Ni_3Al + TiC_x + Ti_3AlC_2/Ti_3AlC_2$. As the bonding temperature increased, the thickness of Tiss in TiAl/Ti interface gradually reduced, the Ti_3Al intermetallic layer gradually thickened, and the thickness of TiNi intermetallic layer increased significantly, while the thickness of Ti_2Ni and Ni_3Ti intermetallics layers remained substantially constant. The shear strength of joints first increased and then decreased with increasing the bonding temperature. The maximum shear strength of the joint can reach 85.3 MPa when bonded at 850 ℃. The joint fracture occurred mainly in Ni/Ti_3AlC_2 interface and Ti_3AlC_2 matrix.

Key words: TiAl alloy; ceramic; diffusion bonding; interfacial microstructure

Study on phase matching control system for pulsed laser-arc hybrid welding based on Labview

SONG Gang, LIU Che, SONG Qiuping, LIU Liming (Key Laboratory of Liaoning Advanced Welding and Joining Technology, School of Materials Science and Engineering, Dalian University of Technology, Dalian 116024, China). pp 13 - 16

Abstract: This article introduced a pulsed laser-arc hybrid welding phase matching control system based on Labview. Using NI's PCI6221 data acquisition card, the DAQ system acquired current of AC arc signal, processed the signal and capture the feature points of arc by the computer, thus accurately analyzed the phase of AC arc, and realized a continuous trigger control of pulsed laser on specific phase of AC arc. The locking trigger method was put forward, which eliminated the wrong trigger of laser, realized frequency doubling of pulsed laser and arc and trigger frequency protection of laser. The verifying experiment indicated that the system realized a accurately trigger control of specific phase of arc and the pulsed laser, and also provided the technical support of flexible combination of energy of pulsed laser and AC arc and the research on mechanism of interaction between the two heat resource.

Key words: welding; laser-arc hybrid welding; phase matching; control system

Numerical analysis of three-wire tandem submerged arc welding grade X80 pipeline steel

ZHAO Ming, WANG Haiyan, WAN Fuwei, LUO Detong (College of Mechanical and Electronic Engineering, China University of Petroleum, Qingdao 266580, China). pp 17 - 20

Abstract: A model for the thermal process in three-wire

tandem submerged arc welding of grade X80 pipeline steel is developed by using finite element analysis software ANSYS. The element birth-death technique is employed to deal with the filling of double-V groove along the longitudinal seam of pipeline steel, and double-ellipsoid volumetric heat source is used to achieve the thermo-load application and solution. The calculated results show that the phenomenon, three-wire in a single weld pool, emerges at 1.6 s after the weld starting, the quasi-steady state is achieved at 6 s, and then a weld pool with length of over 100 mm is produced. The three peak values of temperature at the thermal cycles in weld and heat affected zone elongate the high temperature dwelling time of the thermal cycles, which is the main reason why the grains in the heat affected zone become coarser and the joint properties worsen. The comparison between the experimental and predicted results shows that the agreement extent of the weld width is better than that of the weld penetration, and the calculation accuracy can be improved if the weld reinforcement is considered.

Key words: pipeline steel; multi-wire tandem submerged arc welding; heat affected zone; thermal cycle; numerical simulation

Research on rapid underwater welding based on SHS

YIN Yujun, PAN Chuanzeng, SU Shan (Department of Vehicle and Electric Engineering, Mechanical Engineering College, Shijiazhuang 050003, China). pp 21 – 24

Abstract: Based on SHS technology, rapid underwater welding was investigated. The solder was composed of thermite of $CuO + Cu_2O + Al$, gasification agent of $CaCO_3$, alloy agent of $FeSi + MnFe$ and slagging agents of B_2O_3. The weld block was consisted of graphite crucible and rectangular pipe, meanwhile, one end of rectangular pipe was sealed and another one sealed partly to control the heating direction of combustion flame. Tungsten coil was used to ignite KNO_3/Al-Mg ignition materials and the paraffin was used to seal the opening of the weld block. Finally, the feasibility problem of underwater welding based on SHS was solved. It was found that, this technology can be operated easily without power supply to form welded joints after self-combustion of the solder in weld block. Welded joints with tensile strength of 135 MPa can be obtained under the condition of water depth of 0.5 m, and the emergency repairs of underwater damaged structures can be realized basically.

Key words: underwater welding; self-propagation; emergency repairs; welding mechanism

Microstructure and mechanical properties of variable polarity plasma arc keyhole weld of 2A12 aluminum alloy

JIANG Yi[1,2], LIU Ming[2], LU Yaohui[2], XU Binshi[2] (1. Logistics academy, Naval University of Engineering, Tianjin 300450, China; 2. National Key Laboratory for Remanufacturing, Academy of Armored Forces Engineering, Beijing 100072, China). pp 25 – 28

Abstract: Variable polarity plasma arc welding, an efficient and cost-efficient welding technology, has been widely applied to aircraft components manufacture, especially aluminum alloy components. Variable polarity plasma arc keyhole weld of 2A12 aluminum alloy was conducted by welding torch with assistant nozzles under high welding speed and high heat input, and microstructure and mechanical properties of weld zone was analyzed as well. Due to the compression of assistant nozzles to plasma arc, crown weld is narrowed, however, root weld is broadened; reinforcements of both welds are increased. In the weld, fine equiaxed nondendritic grains are dominate, strengthening phases are with Al_2Cu phases largely and few S phases. Mechanical properties of weld zone are determined by the size and quantity of Al_2Cu. It could be concluded that the difference of hardness between parent metal and weld is little. Furthermore, microhardness distribution curve alongside longitudinal direction of weld is like U-shape, plain in the middle of weld and fluctuating in both sides of the crown and root weld.

Key words: variable polarity plasma arc; aluminum alloy; keyhole weld; mechanical properties

Influence of welding residual stresses on fatigue life of Al 2024 plate

ZHANG Zhengwei, ZHANG Zhao, ZHANG Hongwu (State Key Laboratory of Structural Analysis for Industrial Equipments, Dalian University of Technology, Dalian 116024, China). pp 29 – 32, 36

Abstract: Sequential coupled thermo-mechanical model and fracture mechanical model based on finite element method and J-integral method are established to calculate the residual stress and the stress intensity factor for friction stir welding, TIG and laser welding process, respectively. The commerical code NASGRO is used to predict the fatigue crack growth rate. This method is validated by comparing with the experimental data and results of the virtual crack closure technique method. The distribution of the residual stress intensity factor is similar with the residual stress profile and the residual stress has a significant impact on the effective stress ratio R. The influence decreases as the increase of the stress ratio. The residual stresses severely shorten the fatigue life of the plate, and the fatigue life of the plate welded with TIG technology is shorter than the ones of the plates welded with friction stir welding and laser welding.

Key words: welding residual stresses; J-intergral; residual stress intensity factor; fatigue crack growth rate

Preparation and connectivity of sintering paste containing copper particles covered by nano-silver

CAO Yang[1,2], LIU Ping[1], WEI Hongmei[2], LIN Tiesong[2], HE Peng[2], GU Xiaolong[1] (1. Zhejiang Province Key Laboratory of Soldering & Brazing Materials and Technology, Zhejiang Metallurgical Research Institute Co. Ltd., Hangzhou 310030, China; 2. State Key Laboratory of Advanced Welding and Joining, Harbin Institute of Technology, Harbin 150001, China). pp 33 – 36

Abstract: A kind of sintering paste mixed of nano-silver and copper particles covered by nano-silver was made, by which oxygen-free copper pad with 99.99% purity were connected at low temperature. Firstly, nano-silver particles whose average diameter were 20 – 35 nm were synthesized by liquid chemical reduction method. Meanwhile the copper particles covered by nano-silver were prepared by the method of chemical plating. Afterwards, these two kinds of particles were mixed by mechanical method to prepare sintering paste, by which oxygen free copper plate with 99.99% purity were joined under the condition of 10 MPa, 200 ℃ for 30 min. Finally, the microstructure of sintering section was observed by the scanning electron microscope (SEM). The results showed that the connection interface was sintered compactly, and certain porosities existed throughout the joint organization. The everge shear strength of the joints was about 20 MPa.

Key words: nano-silver; copper particles covered by nano-silver; low temperature connection